

The effect of the interface on coupling wind and wave modeling

Jianting Du Xiaoli Guo Larsén Rodolfo Bolaños
Mark Kelly Merete Badger Søren Larsen

February 17, 2017

Abstract

1 Introduction

Air and sea interact, with wind generating waves and waves influencing the wind field. This topic is ever relevant for offshore functions e.g. shipping, offshore foundations, wind farm operation, maintenance and design. While it is accepted that an improved wind input results in improved wave modeling, the wave impact on the wind modeling has not been as conclusive. Numerical experiments sometimes found considerable or noticeable difference introduced by a wind and wave coupled system in comparison with a non-coupled system, e.g. hurricane strength and track by [1] who added the spectral tail to the current wave models. However, more often it has been reported that this impact is too small, which raised the question if we need a coupled system to model the wind offshore.

1.1 The interface using the roughness length

In numerical experiments, often the atmospheric model and the wave model are coupled through an interface defined through the roughness length z_0 . Mostly, z_0 is described through the Charnock relation [2]:

$$z_0 = \alpha u_*^2 / g \tag{1}$$

where α is the Charnock “constant”, and u_* is the friction velocity and g is the gravitational acceleration.

The Charnock relation should only work for fully developed wind sea for open ocean conditions and the Charnock “constant” has been found to vary with sea state related parameters. In the past decades there have been considerable amount of work, both from atmospheric and wave modeling communities, addressing this interface parameter z_0 in terms of the Charnock constant. The often cited and used schemes include those from Drennan et al. [3], Fan et al. [4], Liu et al. [5], Oost et al. [6], Taylor and Yelland [7] and Andreas et al. as in SWAN.

In the Drennan scheme, z_0 is parameterized through the significant wave height H_s and the inverse wave age u_*/c_p , with c_p the wave phase velocity at the peak frequency of the wave spectrum:

$$z_0 = 3.35H_s(u_*/c_p)^{3.4} + 0.11\nu/u_* \quad (2)$$

where ν is the viscosity coefficient. The second term of the right hand side of Eq. (2) describes the contribution from smooth flow to the roughness length, which is important only at light winds e.g. the 10 m mean wind speed $U_{10} < 3 \text{ ms}^{-1}$.

The Fan scheme [4] includes the smooth flow contribution and a Charnock formulation base:

$$z_0 = \alpha u_*^2/g + 0.11\nu/u_* \quad (3)$$

Here the Charnock parameter α is parameterized with the wave age c_p/u_* :

$$\alpha = a(c_p/u_*)^{-b} \quad (4)$$

where

$$a = \frac{0.023}{1.0568U_{10}}, \quad b = 0.012U_{10}. \quad (5)$$

The Liu’s scheme [5] has the same base format as Eq. (3); here α is also parameterized through the wave age c_p/u_* , but in a different form from the Fan formulation Eq. (4). For young waves, $0.35 < c_p/u_* < 35$:

$$\alpha = (0.085(c_p/u_*)^{3/2})^{1-1/\omega} (0.03c_p/u_* \exp(-0.14c_p/u_*))^{1/\omega} \quad (6)$$

and for old waves $c_p/u_* > 35$:

$$\alpha = 17.61^{1-1/\omega} 0.008^{1/\omega}, \quad (7)$$

where $\omega = \min(1, a_{cr}/(\kappa u_*))$, with $a_{cr} = 0.64 \text{ ms}^{-1}$, and κ is the von Karman constant 0.4.

Table 1: Details about the 5 schemes.

scheme	validation measurements	U_{10} range (ms^{-1})
Taylor-Yelland	HEXMAX,RASEX,Lake Ontario	2 – 20
Drennan	FETCH,WAVES,AGILE SWADE,HEXOS	2 – 20
Oost	ASGAMAGE	1 – 20
Fan	Drennan,CBLAST,Powell	10 – 50
Liu	Jones and Toba 2001	–

Oost et al. [6] parameterizes z_0 in terms of the wave length at the peak frequency, L_p , and the inverse wave age u_*/c_p :

$$z_0 = \frac{50}{2\pi} L_p \left(\frac{u_*}{c_p}\right)^{4.5} + 0.11\nu/u_* \quad (8)$$

The Taylor and Yelland [7] formulation reads:

$$z_0 = 1200 H_s (H_s/L_p)^{4.5} \quad (9)$$

where H_s/L_p represents the wave steepness.

By examining thousands of eddy-covariance measurements of the air-sea surface stress, [8] found the following simple description to be useful up to U_{10} of about 25 ms^{-1} :

$$z_0 = z \exp(-u_*/U_{10}) \quad (10)$$

where $z = 10 \text{ m}$, and u_* and U_{10} are bounded by the following relationship:

$$u_* = 0.239 + 0.0433 \left((U_{10} - 8.271) + \sqrt{0.12(U_{10} - 8.271)^2 + 0.181} \right) \quad (11)$$

The above derivations have been validated with measurements from various places, with most representing open water conditions, see Table 1 for details. The behaviors of z_0 in the coastal zones could be different from the open water conditions, due to factors such as fetch, stability under the impact of upwind land, bathymetry, shoaling and wave breaking processes (e.g. [9]).

1.2 The interface using wave boundary layer model

The limitations in using the roughness length as the exchange parameter between wind and wave modeling are seen to include: (1) the derived wave parameters such as H_s , c_p and L_p , smear out the tremendous calculation effort in wave modeling, especially for challenging conditions in the coastal

shallow zones with fetch influences. Through z_0 that is described with these derived parameters, the wave effects may not be efficiently transported to the atmospheric model. (2) The parameterizations of z_0 have only been validated in certain conditions of wind speed ($U_{10} < 30 \text{ ms}^{-1}$), most of which are deep water and open sea conditions. (3) The set of stress and z_0 in the atmospheric modeling and those in the wave modeling are not necessarily calculated using the same algorithms, due to the post-processing procedures that are done separately in the two model components, thus introducing inconsistency.

The Janssen scheme [10] differs from the above derivations since it does not use the derived parameters such as c_p , H_s or L_p . Rather, it describes z_0 using the wave-induced stress τ_w that is calculated from the wind input through the wave balance equation:

$$z_0 = \frac{0.01u_*^2}{g\sqrt{1 - \tau_w/\tau}} \quad (12)$$

Referring to Eq. (1), Eq. (12) implies that, when the wave-induced stress τ_w becomes comparable to the total stress τ in the surface layer, for instance in the presence of young wind sea, an enhancement in the Charnock value occurs, indicating a more efficient momentum transfer from air to water.

However, it has been reported that Janssen (1991) overestimates the wind stress in strong-wind conditions (Jensen et al. 2006). The overestimation was also found in WAVE-WATCH III when using other wind-input source terms according to Moon et al. (2004, 2009). One of the attempts to deal with this issue is to use a cap to limit u_*/U_{10} within a certain range (Jensen et al. 2006). Another attempt is to reduce the growth rate by introducing the sheltering effect of the low frequency waves (e.g., Makin and Mastenbroek, 1996; Kudryavtsev et al., 1999; Chen and Belcher, 2000; Hara and Belcher, 2002; Makin et al., 2007). For this, some used the wave boundary layer model (WBLM) (Makin and Mastenbroek, 1996; Hara and Belcher, 2002, 2004; Moon et al., 2004). The WBLM takes into account of the momentum conservation and sheltering effect and at the same time ensures that the turbulent kinetic energy (TKE) conserves at all model levels in the WBL. Several studies showed improvements in wave modeling through using WBLM (Moon et al. 2004; Tolman and Chalikov 1996; Chen and Yu 2016).

However, the above mentioned studies used WBLM ahead of the wave modeling but did not use it as a wind-input source function for the wave model, so that the wave growth within the WBLM is not consistent with the wave growth in the wave model. This means that, numerically, the momentum loss from the atmosphere is not exactly the same as the momentum

gained by the waves. To solve this problem, [11] introduced the WBLM to the Janssen 1991 wind-input source function in SWAN, so that the WBLM and the wave model share the same wind-input source function, thus ensuring the momentum flux is consistent at the interface of atmospheric and wave model. The new pair of wind-input and dissipation source functions in [11] have shown improved wave simulation as well as the dependence of the drag on wind speed for a wide range of conditions of wind speed, wave state and fetch.

1.3 Purpose of this study

We investigate the effect of various interfaces for the wind-wave coupling modeling system on the wind and wave field, with the focus on the wind field. The purpose is to gain a better understanding of the efficiency and accuracy of information exchange between two model components with these different interfaces.

The methods are described in section 2, where firstly the studied cases are introduced in section 2.1, followed by introduction of the measurements and modeling in sections 2.2 and 2.3. Here we use the Weather Research and Forecasting (WRF) model and the spectral wave model for near shore (SWAN) in the coupled-ocean-atmosphere-wave-sediment transport (COAWST) modeling system. Results are presented in section 3. Discussions and conclusions follow in sections 4 and 5.

2 Method

This study was motivated by a SAR (Synthetic Aperture Radar) image shown here in Fig. 1 which is from 9:50 am on 2004-02-23; Fig. 1b is a closeup of Fig. 1a over an area around Horns Rev 1. The wind at this time is from the north sector; at Horns Rev 1 mast 2 (M2) site, the wind speed at 15 m changed from about 8 to 10 ms^{-1} with a direction from 0 to 15° (see more details in section 2.2). The SAR winds at 10 m close to M2 show comparable wind strength to the mast measurements, although the spatial variation of the wind speed nearby is significant. SAR utilizes the fact that radar backscatter from the sea surface depends on centimeter-scale waves that are generated by winds locally. Although earlier studies have shown that statistically the SAR winds from the area of Fig. 1b are of reliable quality in comparison with mast measurements, it is difficult to quantify the quality of the SAR winds for any particular pixel in this particular picture. Nevertheless, the SAR wind field in Fig. 1b reflects the pattern of the local

bathymetry, which is plotted in Fig. 2, implying that the wind waves were affected by the bathymetry and they modified the wind field.

Fig. 1b can be qualified as an evidence that the waves affected the wind field.

The investigation of the impact from the interfaces on the wind and wave field is conducted through case studies. The focused areas include the one shown in Fig. 1 for its coastal features and the one close to the storm center for the strong winds there.

The model is run in both coupled and non-coupled modes. The coupled mode includes coupling using direct stress transport through the interface using WBLM and coupling using parameterized z_0 as the interface. Five schemes as described in section 1.1 and listed in Table 1 are used for parameterizing z_0 and they are referred to as: (1) Taylor and Yelland; (2) Drennan; (3) Oost; (4) Fan; (5) Liu. The non-coupled modeling uses the default description of the roughness length in WRF, which is called COARE 3.0. As will be shown in section 3, the expression from Andreas et al. [8], Eq.s 10 and 11 are basically the same as that from COARE 3.0 for $U_{10} > 10 \text{ ms}^{-1}$ and it is therefore not included in the analysis.

The numerical experiments have been done mostly to the case related to Fig. 1. The meteorological background related to this case, together with another relevant case, is introduced in section 2.1. The analysis and evaluation of the numerical experiments use measurements from the Horns Rev 1 site (section 2.2). The modeling system is described in section 2.3.

2.1 The cases

Two cases are analyzed here. Case 1 is from 2004-02-22 to 2004-02-24. Case 2 is from 2002-01-27 to 2002-01-29.

Fig. 1 is during case 1. The wind field shown in Fig. 1 corresponds to a passing storm and by the time of Fig. 1, 9:50 am on the 23rd, the storm center is close to ($69^\circ N, 5^\circ W$), according to the cloud pictures (<http://www.sat.dundee.ac.uk>). At Horns Rev 1, at 9:50 am on the 23rd, the storm has already past the peak strength, see the time series of various variables in Fig. 6. The first reason for us to choose this case is the message in the SAR data over Horns Rev 1 that the wind field is affected by the waves, which is against the popular speculation in the modeling community that the surface waves do not affect the wind. This is seen as a good opportunity to examine the reactions of the various ways of wave input to the atmospheric modeling. Another important reason to choose this case is that measurements of standard meteorological parameters, turbulence and waves are available (see section 2.2).

At M2, the strongest wind speed during case 1 is moderate, about 15 ms^{-1}

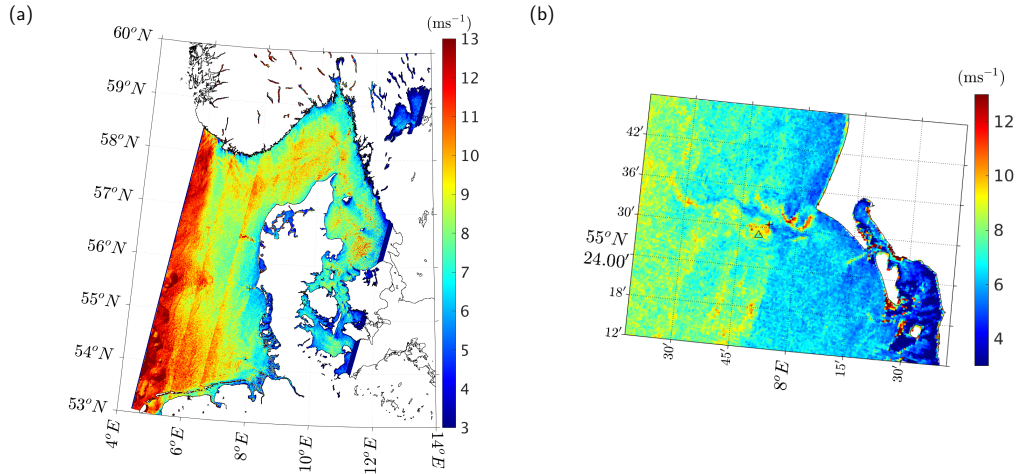


Figure 1: The 10 m wind speed from SAR at 9:50 on 2004-02-23, unit ms^{-1} . The pixel size is 500 m by 500 m. (a) over a bigger area (b) closeup to Horns Rev 1

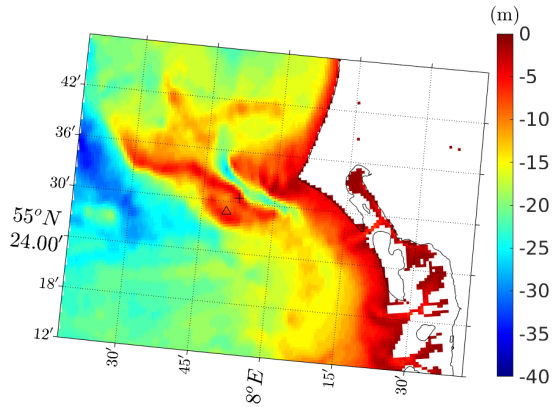


Figure 2: The bathymetry around Horns Rev in meter. The resolution is 200 m. The cross and the triangle show the positions of M2 and buoy, respectively. Jianting: We need details of the data in the text.

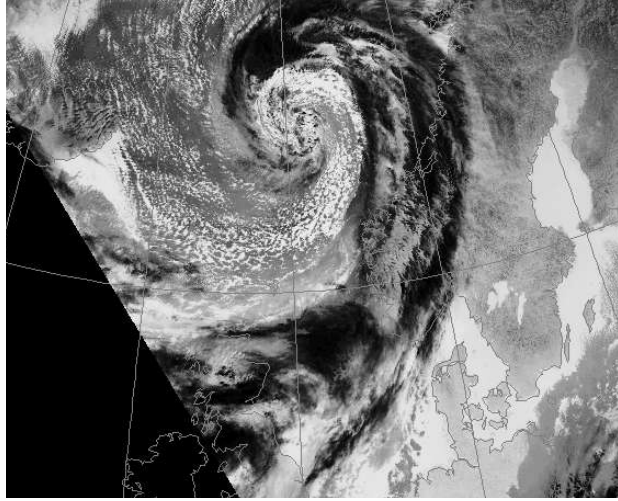


Figure 3: Cloud picture showing the storm center around (66°N,2°W) at 20:45, 2004-02-23.

at 10 m, but not strong. It is expected to be more challenging to describe the waves at strong winds such as U_{10} of 25 ms^{-1} and large diversity in z_0 between the different approaches are expected. In order to see this effect, case 2 is introduced. During case 2, the storm center past the west coast of Denmark and it was rather close to our measurement site.

2.2 Measurements

We used cloud pictures, SAR images, mast and buoy measurements from Horns Rev 1 in this study. The SAR images provide us a overview of spatial distribution of the wind field, with details of special features and patterns. However the images are rare over a particular area. Cloud pictures are useful for an overview of the structure of a storm, its size, the track the storm center, and special mesoscale patterns such as the open cells. Here in Figure 3 which is at 20:45 on the 23rd, the storm center and mesoscale features can be seen.

The measurements from Horns Rev 1 are from 1999 to 2006. The locations of M2 and the buoy are shown in Fig. 1b and Fig. 2 as plus and triangle, respectively. The complete set of meteorological (10-min averages and turbulence) and wave data allows us to examine the general validity of the many schemes for the roughness description, statistically as well as case wise.

The standard meteorological measurements at M2 include wind speeds

at 15 m, 30 m, 45 m and 62 m, directions at 43 m and 60 m, temperatures at 13 m and 55 m. The sonic has been mounted at 50 m, providing data for momentum and sensible heat fluxes. Water temperature was measured 4 m beneath water surface.

Horns Rev is a coastal site. The water depth at this site varies from 6 to 12 m. According to the distribution of the ratio of water depth (D) and the peak wave length (L_p), D/L_p , the site can be considered as intermediate to shallow water [12]. The wave measurements were made through a Wave Rider buoy and the details of the measurements can be found in [13]. The waves were measured through the vertical acceleration of the buoy. As the buoy follows the waves, the force of the mooring line will change. The force is produced by the changing immersion of the buoy, resulting in an error of 1.5% maximum [14]. The significant wave height H_s was derived from a 1D wave power spectrum measured by the buoy. The data are available from July 1999 to June 2006, half hourly. Data analysis was done in [13] for the year 2004 where the data quality was considered to be reliable. Similar data examination was done here for 1999 to 2006 and we did not find any abnormal data distribution behaviors and therefore conclude that the data quality is fine.

There are two reasons that we use the Monin-Obukhov Similarity Theory (MOST), rather than the Charnock formulation, to calculate z_0 and the drag coefficient C_D from the measurements for the Horns Rev site. Firstly, the measurement of the momentum fluxes and hence u_* is at 50 m, rather than 10 m as required in Eq. (1); one would need a model for the height dependence of u_* for that purpose. Secondly, we want to avoid parameterization but rather use the definition of z_0 directly through MOST.

The validity of MOST needs to be proven in order to ensure the credibility of the calculation of z_0 and hence C_D . For this, we examine if the non-dimensional wind gradient ϕ_m is well described in terms of the stability parameter z/L with $z = 50$ m, where

$$\phi_m = \frac{\kappa z}{u_*} \cdot \frac{\partial U}{\partial z}, \quad (13)$$

and the Obukhov length L :

$$L = -\frac{\theta u_*^3}{\kappa g w' \theta'}, \quad (14)$$

with $\partial U/\partial z$ calculated from the second-order polynomially fitted curve to the wind measurements at 15 m, 30 m, 45 m and 62 m. Note, here the temperature θ , sensible heat flux $\overline{w'\theta'}$, u_* and the wind gradient $\partial U/\partial z$ are all referring to $z = 50$ m.

In Fig. 4, two groups of data, one with onshore flow (Fig. 4a) and one with offshore flow (Fig. 4b) show that the widely accepted formulations for describing the $\phi_m - z/L$ relation are valid. Note that here the gray and black dots correspond to data with wind speed greater than 10 ms^{-1} at 62 m and 15 m, respectively. Including lower wind speeds gives larger scatter but does not change the statistics. The $\phi_m - z/L$ relations are often described with MOST as:

$$\phi_m = (1 - C_1 z/L)^{-1/4} \quad z/L \leq 0 \quad (15)$$

and

$$\phi_m = 1 + C_2 z/L \quad z/L \geq 0 \quad (16)$$

or

$$\phi_m = 1 + a_1 \cdot z/L + (1 + c_1 - d_1 \cdot z/L) \cdot z/L \cdot b_1 \exp(-d_1 z/L) \quad z/L \geq 0 \quad (17)$$

for very stable conditions with $a_1 = 0.7$, $b_1 = 0.75$, $c_1 = 5$ and $d_1 = 0.35$ [15]. For our data $C_1 = 19$ and $C_2 = 5$ are satisfactory.

In general, there is more scatter in the offshore flow, likely due to the land impact from upwind land sectors. When the winds are from the land, for very stable condition, Eq. (17) is a better description than Eq. (16). For the onshore flow, such a strong stable stratification effect is absent and Eq. (16) is a good description.

The validity of MOST for the Horns Rev 1 data is supported by Fig. 4, which credits the calculation of z_0 through the following equation given by MOST:

$$z_0 = z \cdot \exp -(\kappa U/u_* + \Psi_m), \quad (18)$$

where Ψ_m is the stability function, for $z/L > 0$:

$$\Psi_m(z/L) = -C_2 z/L \quad (19)$$

and for $z/L < 0$:

$$\Psi_m(z/L) = -2 \ln\left(\frac{1+x}{2}\right) - \ln\left(\frac{1+x^2}{2}\right) + 2 \tan^{-1}(x) - \pi/2, \quad (20)$$

where $x = (1 - C_1 z/L)^{1/4}$.

The drag coefficient C_D is calculated from

$$C_D = \left(\frac{\kappa}{\ln(z/z_0)} \right)^2. \quad (21)$$

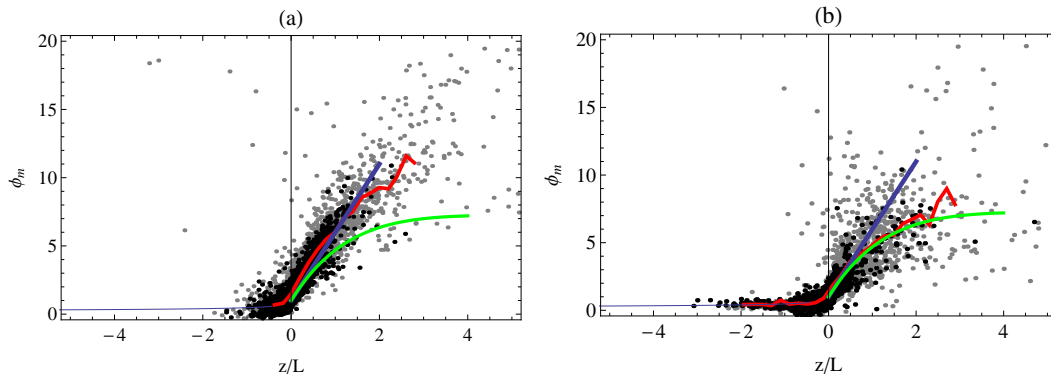


Figure 4: The non-dimensional wind gradient, ϕ_m , as a function of stability z/L , for onshore and offshore wind conditions. Grays dots are for $u > 10 \text{ ms}^{-1}$ at 62 m, and black dots are for $u > 10 \text{ ms}^{-1}$ at 15 m. The red curves are mean values of ϕ_m and z/L , with z/L -bin of 0.2. The blue curves are Eq.s 15 and 16. The green curves are Eq. 17.

The 10 m wind speed is obtained through the second-order polynomially fitted curve to the wind measurements at 15 m, 30 m, 45 m and 62 m.

For the measurements, we also calculated c_p the wave phase velocity at the peak frequency with water depth taken into consideration:

$$c_p = \frac{g}{\omega_p} \tanh\left(\frac{\omega_p D}{c_p}\right) \quad (22)$$

where ω_p is the peak frequency of the wave spectrum and D is the water depth. Wave length L_p is calculated through $L_p = c_p T_p$.

2.3 The modeling system and the WBLM in SWAN

We use the COAWST Modeling System [16] in which the wind (WRF) and wave (SWAN) components are activated. Data exchange between the two model components through the Model Coupling Toolkit (MCT).

The domain setup for WRF and SWAN is the same as shown in Fig. 5. Both have spatial resolutions of 9 km, 3km, and 600 m for three nested domains. There are 77 sigma levels for all WRF domains with the lowest model level at a height of about 5 m. The vertical resolution is about 10 m in the first 100 m above the sea surface. We used MYNN 3.0 PBL scheme [17], Thompson microphysics scheme [18] and RRTM long wave and short wave radiation physics schemes [19] for the three WRF domains. The Kain-Fritsch cumulus scheme [20] is used for domain I, but is deactivated for domain II

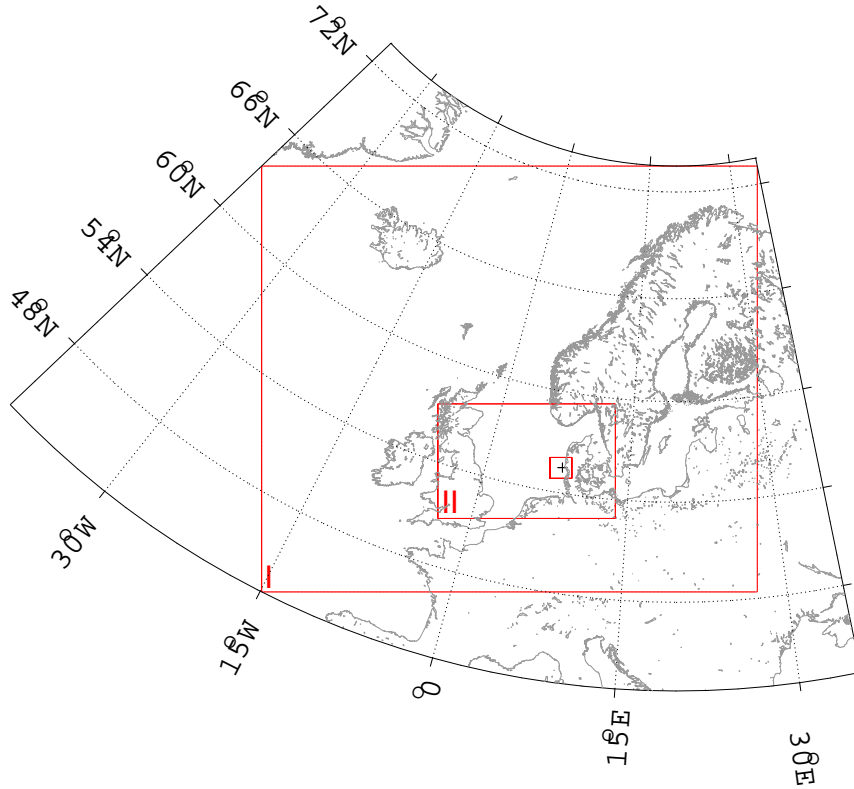


Figure 5: The three nested domains for WRF and SWAN. The two measurement stations of Ekofisk and Horns Rev M2 are marked as black circle and cross in the map.

and III. We used the Climate Forecasting System Reanalysis (CFSR) data for the WRF initial and boundary forcing. The Corine land use data and the NOAA $1/4^\circ$ daily Optimum Interpolation Sea Surface Temperature (OISST) are used.

In SWAN, the $1/8$ arc-minute bathymetry data from the Digital Terrain Model (DTM) of European Marine Observation and Data Network (<http://www.emodnet-hydrography.eu>) was used. For case 1, SWAN is initiated with the output spectrum of a previous SWAN simulation 30 hours ahead of 2004-02-22 06:00:00. The open boundaries of the outer domain are set to zero. We used 36 directional bins. The frequency exponential was 1.1 and the lowest frequency was set to 0.03 Hz. A cut-off frequency of 10.05 Hz in SWAN is chosen so that the wave spectra cover the capillary wave-frequency range.

In the non-coupled simulation, WRF sends the meridional and longitudinal wind components, u_{10} and v_{10} , to SWAN but the wave parameters in SWAN has no impact to the roughness length in WRF.

In the coupled modeling using z_0 from the parameterization schemes, H_s , T_p , and L_p from SWAN are sent to WRF where z_0 is calculated. In SWAN, the Komen wind-input source function for wave growth β_g is used ([?], hereafter KOM):

$$\beta_g(\sigma, \theta) = 0.25\sigma \frac{\rho_a}{\rho_w} \left(28 \frac{u_*}{c} \cos(\theta - \theta_w) - 1 \right) \quad (23)$$

where ρ_a and ρ_w are the air and water density, σ is the radian frequency, θ and θ_w is the wave and wind direction, c is the phase velocity and the friction velocity u_* is calculated from the drag relation $u_*^2 = C_D U_{10}^2$, in which

$$C_D = \left(0.55 + 2.97\tilde{u} - 1.49\tilde{u}^2 \right) \times 10^{-3} \quad (24)$$

according to Zijlema (2012), where $\tilde{u} = U_{10}/31.5(m s^{-1})$.

The details of the WBLM can be found in [11]. Briefly, in the WBLM-coupled simulation, the wave growth rate of Janssen (1991)'s wind-input source function is modified to be proportional to the local turbulent stress $\vec{\tau}_t$, rather than the total stress $\vec{\tau}_{tot}$ at the critical height; the critical height is where c_p equals the wind speed:

$$\beta_g(\sigma, \theta) = C_\beta \sigma \frac{|\vec{\tau}_t(z)|}{\rho_w c^2} \cos^2(\theta - \theta_w) \quad (25)$$

where C_β is the Miles constant, and $\tau_t(z)$ is the local turbulent stress at the critical height which equals to the total stress minus the wave-induced stress:

$$\vec{\tau}_t(z) = \vec{\tau}_{tot} - \vec{\tau}_w(z) = \vec{\tau}_{tot} - \rho_w \int_{\sigma_{min}}^{\sigma_z} \int_{-\pi}^{\pi} \beta_g(\sigma, \theta) \sigma^2 N(\sigma, \theta) \frac{\vec{k}}{k} d\theta d\sigma \quad (26)$$

with $N(\sigma, \theta)$ the action density spectra and k the wave number. The wind profile near the sea surface is expressed as:

$$\begin{cases} \frac{d\vec{u}}{dz} = \frac{u_*}{\kappa z} \frac{\vec{\tau}_{tot}}{|\vec{\tau}_{tot}|}, & z \geq \frac{\delta}{k_{min}} \\ \frac{d\vec{u}}{dz} = \left[\frac{\delta}{z^2} \tilde{F}_w + \frac{\rho_a}{\kappa z} \left| \frac{\vec{\tau}_t(z)}{\rho_a} \right|^{\frac{3}{2}} \right] \times \frac{\vec{\tau}_t(z)}{\vec{\tau}_t(z) \cdot \vec{\tau}_{tot}}, & \frac{\delta}{k_{max}} \leq z < \frac{\delta}{k_{min}} \\ \frac{d\vec{u}}{dz} = \frac{\rho_a}{\kappa z} \left| \frac{\vec{\tau}_\nu}{\rho_a} \right|^{\frac{3}{2}} \times \frac{\vec{\tau}_\nu}{\vec{\tau}_\nu \cdot \vec{\tau}_{tot}}, & z_\nu \leq z < \frac{\delta}{k_{max}} \end{cases} \quad (27)$$

where \tilde{F}_w is the vertical decay function:

$$\tilde{F}_w(\sigma) = \rho_w \int_{-\pi}^{\pi} \beta_g(\sigma, \theta) g \sigma N(\sigma, \theta) d\theta, \quad (28)$$

and k_{min} and k_{max} are the minimum and maximum wave number of the wave spectra. z_ν is the roughness length of the viscous sublayer where the wind speed turns into zero. The wind-input source function, the mean wind profile, and the total stress are calculated explicitly by solving equation (25) to (28) with the boundary condition of the input U_{10} equals the output U_{10} in equation (27). The equivalent z_0 is calculated by equation (18) for neutral condition ($\Psi_m = 0$). At each time step, this z_0 is send to WRF. Here we use 5 minutes as the time step for both SWAN and the coupling.

The white capping dissipation expression of KOM could be written as:

$$S_{ds}(\sigma, \theta) = -C_{ds} \langle \sigma \rangle (\langle k \rangle^2 m_0)^2 \left[(1 - \Delta) \frac{k}{\langle k \rangle} + \Delta \left(\frac{k}{\langle k \rangle} \right)^2 \right] \phi(\sigma, \theta) \quad (29)$$

where $\langle \sigma \rangle$ and $\langle k \rangle$ are the mean wave radian frequency and mean wave number respectively, with $\langle \sigma \rangle = m_0 / \int \int \sigma^{-1} \phi(\sigma, \theta) d\theta d\sigma$ and $\langle k \rangle = \left[m_0 / \int \int k^{-1/2} \phi(\sigma, \theta) d\theta d\sigma \right]^2$, where $m_0 = \int \int \phi(\sigma, \theta) d\theta d\sigma$ is the total wave energy. C_{ds} and Δ are the tuning parameters. For KOM S_{in} (Eq. 23), $C_{ds} = 2.5876$ and $\Delta = 1$.

The white capping dissipation of WBLM uses the same expression as KOM (Eq. 29), with the tuning paramter $\Delta = 0$, it reads

$$C_{ds} = C_{ds}^0 \left(\frac{\tilde{U}_{10}}{15} \right)^{0.8} \quad (30)$$

where $C_{ds}^0 = 2.5876$, \tilde{U}_{10} is a 10 meter wind speed derived from the wind-wave growth relation of Kahma and Calkoen (1992):

$$\tilde{U}_{10} = 8.455 \times 10^5 H_s^3 f_p^5 / g^2 \quad (31)$$

where f_p is the peak frequency of the one dimensional wave spectrum.

Considering the computation time, the Discrete Interaction Approximation (DIA) method (Hasselmann et al. 1985)[?] was used for the non-linear four-wave interactions in all the experiments.

3 Results

3.1 At Horns Rev 1

Figure 6 shows the time series of a number of variables measured at the Horns Rev 1 site during case 1, including wind speed and directions, temperatures of air and water and significant wave height. This site experienced the storm peak before midnight of the 22nd and 23rd of Feb. 2004. The arrow in Fig. 6a shows the time corresponding to Fig. 1.

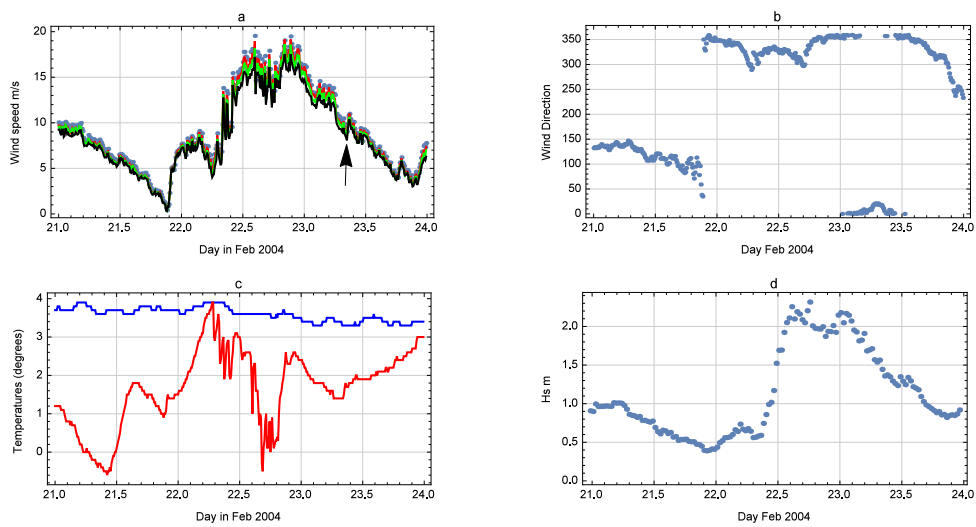


Figure 6: Measured time series of a number of variables from 2004-21 00:00 to 2004-24 00:00 at Horns Rev 1. (a) Wind speeds from M2 at four levels 15 m, 30 m, 45 m and 62 m; (b) Wind direction at M2 and 43 m; (c) Water temperature (blue) and air temperature at 13 m (red); (d) Significant wave height at the buoy close to M2. The arrow in (a) shows the time corresponding to Fig. 1

A series of wave parameters are calculated from the measurements, including H_s , L_p and c_p , making it possible to calculate z_0 from the five schemes in Table 1. The statistics of the wave parameters are presented in Fig. 7a, b, c and d using measurements from 1999 to 2005. In the presentation, the data are divided into two groups according to the wind direction WD , with one group where $180^\circ < WD < 360^\circ$ representing roughly flow from the open water and another group where $0^\circ < WD < 180^\circ$ representing roughly flow from land to water. Figure 7 shows averaged values of c_p/u_* , H_s , H_s/L_p and L_p in 0.5 ms^{-1} bins of U_{10} , for flow from open water and from land to sea, respectively. Note that here u_* is at 50 m, which should statistically be somehow smaller than that at 10 m, so that the wave age here is larger than that by definition. The waves are in general older and higher when the flow is from the sea in comparison with flow from the land. For $U_{10} > 7 \text{ ms}^{-1}$, the waves are also longer but less steep when the wind is from the sea in comparison from the land. However, Fig. 7c and d show that when the wind is weak, the waves are actually steeper and shorter when it is from the sea, in contrast to the strong wind conditions.

Figure 7e and f show the variation of z_0 and C_D with U_{10} for the onshore and offshore flow, respectively. Following the statistics of the wave parameters for the onshore and offshore flow, here the roughness length and drag coefficient dependence on the wind speed are also different. At lower wind speed than 5 ms^{-1} , z_0 and C_D decrease with U_{10} , interpreted by many studies as the smooth flow characteristics. Although it has been shown earlier that considerable uncertainty due to stability correction is involved in the calculation of z_0 and C_D at light winds. For $U_{10} > 5 \text{ ms}^{-1}$, the bin-averaged z_0 and C_D of the onshore flow increase with U_{10} , with considerable scatter when U_{10} reaches about 18 ms^{-1} , due partly to smaller number of samples. This is in consistency with most measurements. For $5 < U_{10} < 12 \text{ ms}^{-1}$, the flow is rougher (higher z_0 and C_D) when it is from the land, which was also observed in [21, 9]. This was interpreted in Sun et al. [22] and Mahrt et al. as the effective roughness length being larger under the impact from land. Note that in their studies, U_{10} of the offshore flow is not more 13 ms^{-1} . However, not like for the onshore flow, z_0 and C_D of the offshore flow did not seem to continue increasing with increasing wind speed when the U_{10} becomes larger than 13 ms^{-1} ; they seem to suggest a saturated momentum exchange at strong winds from land.

3.2 Interfaces: at Horns Rev 1

On top of Fig. 7e and f with $U_{10} > 5 \text{ ms}^{-1}$, in Fig. 8, z_0 was plotted as a function of U_{10} , for the five schemes (Fig. 8a) as well as three main

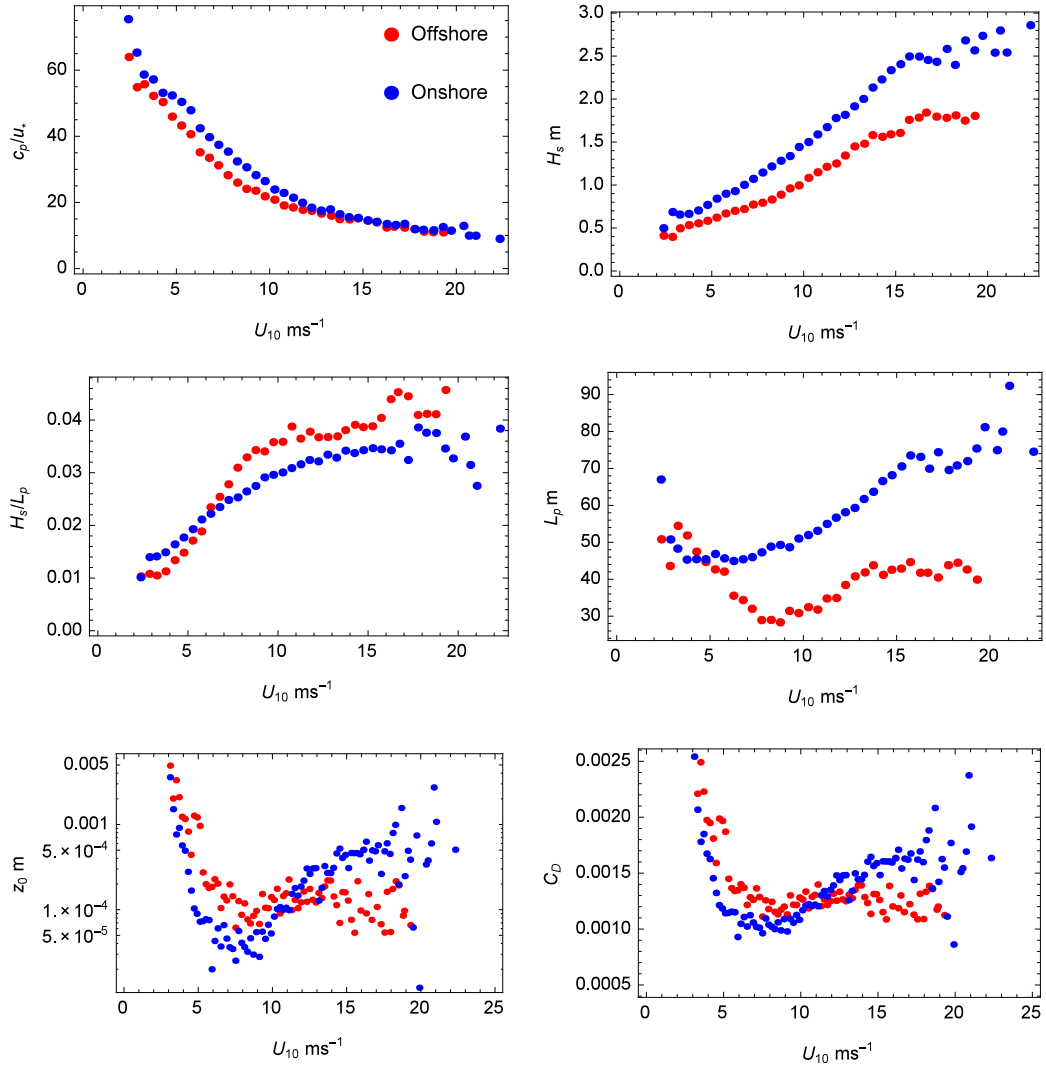


Figure 7: Distribution of a number of variables with mean wind speed at 10 m, U_{10} , in a bin of 0.5 ms^{-1} : (a) wave age c_p/u_* ; (b) significant wave height H_s ; (c) steepness H_s/L_p ; (d) wave length at peak frequency L_p ; (e) roughness length; (f) drag coefficient, for open water flow (blue) and land to sea flow (red).

schemes that are implemented in the WRF model (Fig. 8b). In Fig. 8a, the calculations from the five schemes have been done using bin-averaged wave and wind parameters as shown in Fig. 7a to d. In both subplots of Fig. 8 the algorithm from Andreas [8] is shown and for $U_{10} > 10 \text{ ms}^{-1}$, it is very close to COARE 3.0.

Figure 8a shows that while the different parameterizations give similar estimates of z_0 at light to medium winds, the difference becomes more and more significant as wind speed increases. At $U_{10} \approx 20 \text{ ms}^{-1}$, the Taylor-Yelland scheme gives z_0 of about $5 \cdot 10^{-4} \text{ m}$ while the Oost scheme gives z_0 of about 0.01 m . The WRF calculations are located in-between these schemes (Fig. 8b). Since these schemes have mostly been calibrated with open water flow, the calculations using the two groups of data give negligible differences to the $z_0 - U_{10}$ relation and they are in line with the measurements for the onshore flow. Among them, Taylor-Yelland and Fan give the best agreement for $U_{10} > 10 \text{ ms}^{-1}$, and Drennan, Andreas and COARE 3.0 give the best agreement for $5 < U_{10} < 10 \text{ ms}^{-1}$. Note that we do not have the results from WBLM scheme in this figure since WBLM does not parameterize z_0 , it is therefore case dependent and not suitable for a similar plot. The details of how z_0 from WBLM are given in section 2.3.

Figure 9 shows the modeled time series of the wind speed at 15 m, U_{15} , and H_s through the five interfaces from Table 1, the non-coupled COARE 3.0 algorithm and the WBLM. In agreement with Fig. 8a, when U_{15} is less than about 10 ms^{-1} , the difference in the modeled U_{15} from using different interfaces is very small, e.g. after about 6 am on the 23rd. During this period, the winds are turning from north to northeast, changing from onshore to offshore flow conditions. All predictions of wind speed are slightly overestimated. According to Fig. 8, at Horns Rev 1, when $U_{10} < 12 \text{ ms}^{-1}$, z_0 is in fact larger when the flow is from land than from water. The underestimation in z_0 through the schemes would lead to overestimated wind speed. When the wind speed at 15 m is about 15 ms^{-1} , e.g. between 12 am on the 22nd and 6 am on the 23rd, the difference in the modeled wind speed is as large as 4 ms^{-1} , as a result of the difference schemes for z_0 . During this period, the winds are from the northwest, namely the open sea. According to Fig. 8a, with Oost the largest z_0 and Taylor-Yelland one of the lowest z_0 , the spread and difference of the wind speed is expected. For $U_{15} < 17 \text{ ms}^{-1}$, results from WBLM showed almost no difference to COARE 3.0, likely due to the fact that their corresponding z_0 and C_D are similar in this wind range for winds from the sea.

The significant wave height calculation showed a positive relation to the wind field for the all the parameterization schemes; at the storm peak, where the difference of 4 ms^{-1} in U_{15} gives a difference in H_s of about 0.2 m .

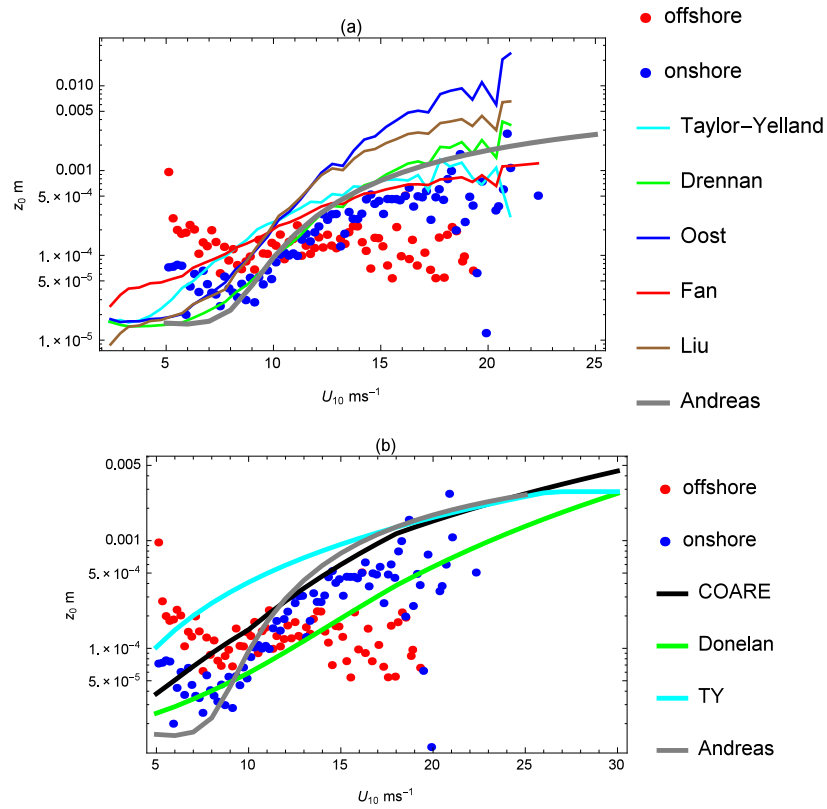


Figure 8: (a): Roughness length calculated with measurements from Horns Rev 1 with various schemes, together with measurements, for Horns Rev 1. (b): three roughness length descriptions in the WRF model, together with measurements, also for Horns Rev 1.

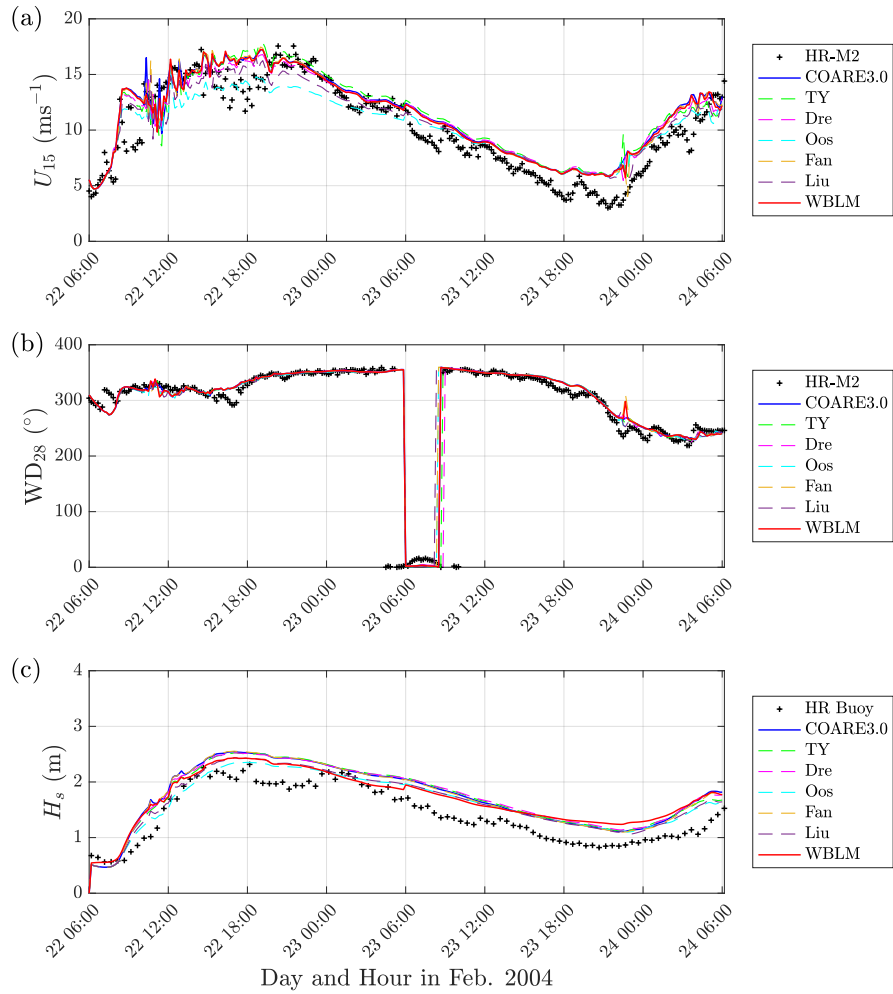


Figure 9: Measured and modeled time series of (a) wind speeds at 15 m (b) wind directions at 28 m (c) significant wave height, during 2004-02-22 and 2004-02-23, at Horns Rev M2, from domain III.

3.3 Interfaces: spatial distribution of wind

Based on Fig. 8 we expect larger difference in z_0 at stronger winds from the different parameterizations. During this storm, the storm center has been in the Atlantic Ocean, being far away from the Danish coast and our model domain III. The wind fields from domain I and II are therefore also analyzed.

Around the wind peak at Horns Rev 1, the wind speed differs not only in the time series as shown in Fig. 9 as a result of the schemes for z_0 , but also in the spatial distribution. Figure 10 shows the spatial distribution of U_{10} for the range 13 to 15 ms^{-1} from the seven schemes at 00:00 on 23rd, right after the storm peak. Oost and Liu provide in general smaller wind speed, due to larger z_0 values. Fan and COARE 3.0 are quite similar. The non-coupled scheme, COARE 3.0, does not give the pattern of the bathymetry, while all the others do, with some more dominant (e.g. Taylor-Yelland, Drennan, Oost) than the others (e.g. Fan, Liu and WBLM). The pattern featuring the bathymetry is also present in the fields of u_* and z_0 ; here we plot z_0 in Fig. 11. Three of the schemes, Drennan, Oost and Liu have enhanced momentum where the water level is shallow (larger u_* and z_0), while Taylor-Yelland, Fan and WBLM show a consistent picture that the stress transfer is less efficient (smaller u_* and z_0) in the shallow waters.

At 9:50 am, the time corresponding to that of the SAR image in Fig. 1, the pattern of the bathymetry is also present in the modeled fields of u_* and z_0 , but only vaguely in the wind speed field from the schemes of Taylor-Yelland, Drennan, Oost and Liu and almost invisible from Fan and WBLM, see Fig. 12. Seemingly, in the modeling, this effect of waves is mostly obvious in strong wind conditions.

In the following the wave impact is examined through the analysis of the drag coefficient. In COARE 3.0, the wave impact is absent and the drag coefficient is a function of wind speed only, shown as a clear curve for the $C_D - U_{10}$ relation.

The coupling interfaces introduce a spread of C_D at each wind speed due to the involvement of wave parameters. Fig. 13 shows the variation of C_D with U_{10} at all grid points in domain III at the snapshot at 00:00, 2004-02-23. Together shown are the COARE 3.0 relation, the empirical curve from Zijlema [?] and measurements from the studies of Soloviev et al. (triangles), Balck et al. (squares), Donelan et al. (diamonds) and Powell et al. (circles). The Fan scheme shows least spread of C_D , being most similar to COARE 3.0. WBLM provides the distribution of C_D with U_{10} most close to that of measurements. In the plots, the purple curves are mean values of C_D in bins of U_{10} of every 0.2 ms^{-1} , denoted here $C_{D,a}$ (Jianting: is it 0.2 m/s?). During case 1 over domain III, the wind speed at 10 m is maximally about 15 ms^{-1} ;

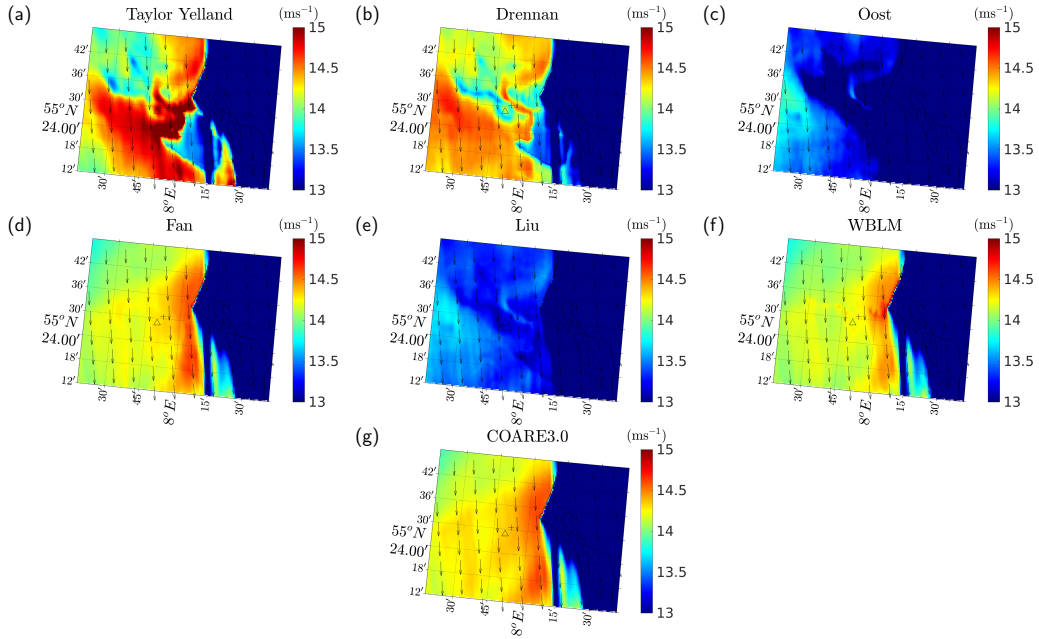


Figure 10: Modeled wind speed at 10 m over domain III at 00:00, 2004-02-23, from the various schemes.)

the $C_{D,a} - U_{10}$ relations from Taylor-Yelland, Fan and WBLM are comparable to the COARE relation, and the rest three show larger $C_{D,a}$ values at the same U_{10} .

To include stronger winds into the analysis, we examine the drag coefficient around the storm center that is present in domain I. In Fig. 14, the difference between C_D and $C_{D,a}$ from domain I is plotted around the storm center at the time of the cloud picture Fig. 3. One can see that the storm center in our simulation agrees well with the cloud picture, at around ($66^\circ\text{N}, 2^\circ\text{W}$). The difference between C_D and $C_{D,a}$ is expected to reflect the spatial distribution of wave impact as described by the six interfaces. Correspondingly, the differences in U_{10} , in the coupled ($U_{10,cou}$) and non-coupled ($U_{10,ncou}$) modeling, around the storm center are shown in Fig. 15 in percentage ($r = (U_{10,cou} - U_{10,ncou})/U_{10,ncou}$). The difference r can be larger than 10%. For Oost and Liu, due to that z_0 and C_D are in general significantly larger than the COARE3.0 values, the winds are on average smaller, except for a few places. WBLM shows closest results to the COARE 3.0 results, although there are places around the storm center the difference can be as large as 10% (or is it more like 8%?) (Fig. 15f).

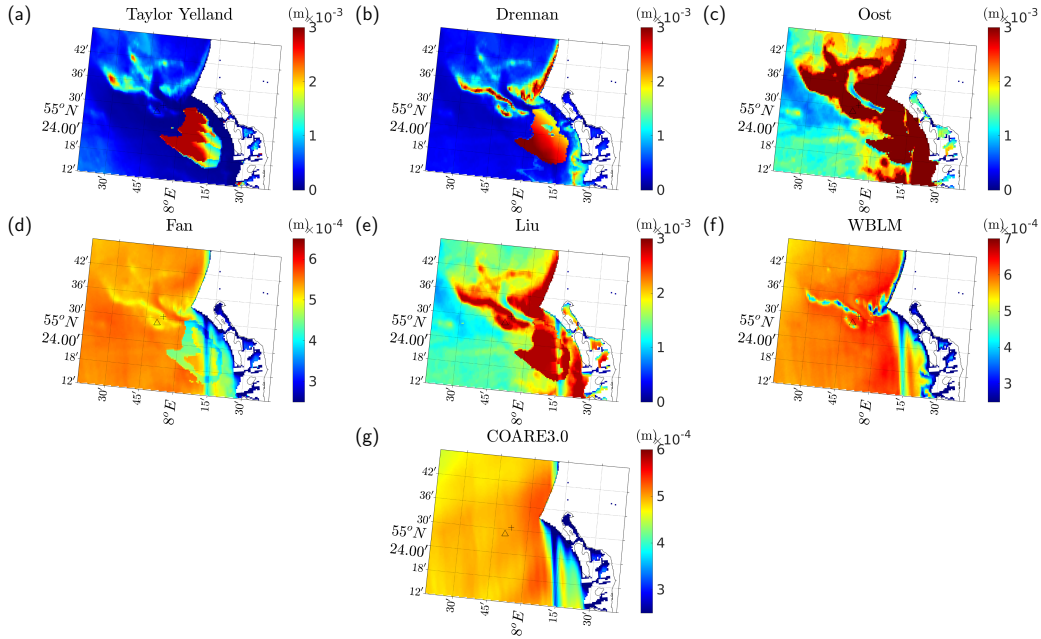


Figure 11: Roughness length z_0 (m) over domain III at 00:00 on 23rd, 2004. (a) not coupled; (b)-(f) the five schemes; (g) calculated from WBLM.

3.4 Case 2: spatial distribution around Horns Rev 1

As introduced earlier that case 1 had the storm center rather far away from the Horns Rev 1 site and the winds at Horns Rev 1 did not become very strong. During case 2 the storm center was rather close to Horns Rev 1, see Fig. 16a and the recorded wind speed at 15 m at Horns Rev 1 reached 27 ms^{-1} . Figure 16b suggests that the effect of introducing the wave contribution seems having affected the calculation of winds both over land and over water. The difference between using WBLM and COARE 3.0 can be as big as 10%.

Over domain III, as Fig. 1b, using COARE 3.0 will not show the presence of bathymetry, as expected, while using WBLM does (Fig. 17a and b). Over shallower waters, WBLM suggests an increase of U_{10} of 6%, see Fig. 17c, as a result of the wave impact.

4 Discussions

This study, for the first time, implements several most often used parameterization schemes for z_0 as the interface for wind and wave coupled modeling,

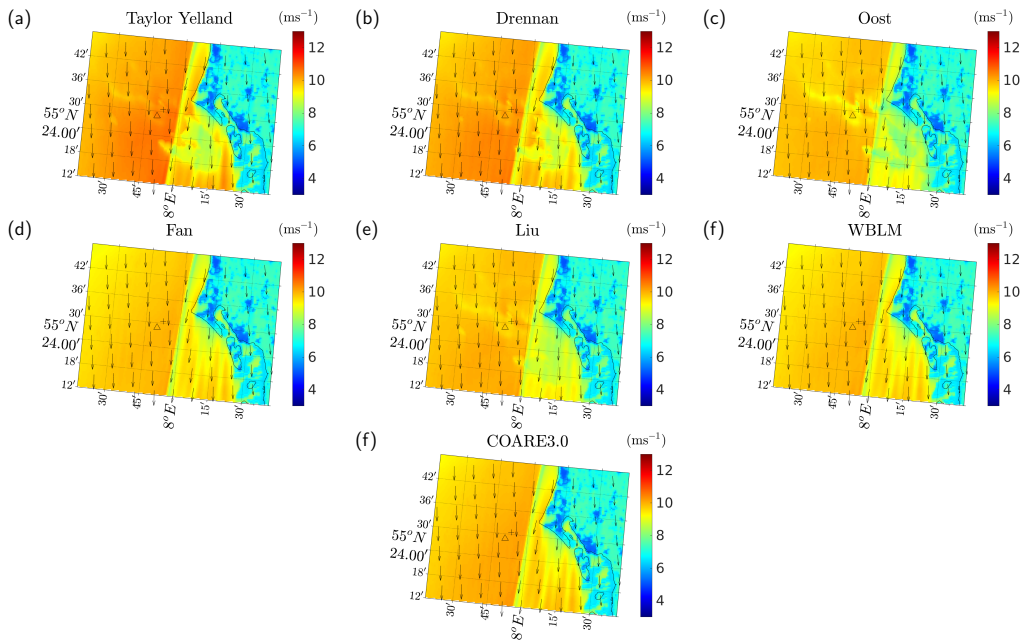


Figure 12: Modeled wind speed at 10 m over domain III at 09:50, 2004-02-23, from the various schemes.)

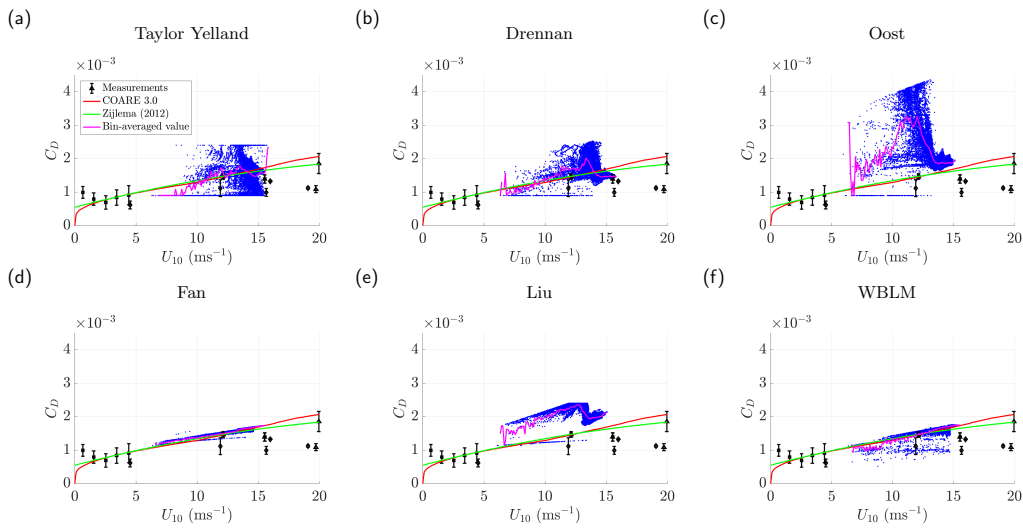


Figure 13: The drag coefficient as a function of wind speed at 10 m from various schemes. The COARE scheme is the red curve in each subplot. Jianting: specify where the measurements are from.)

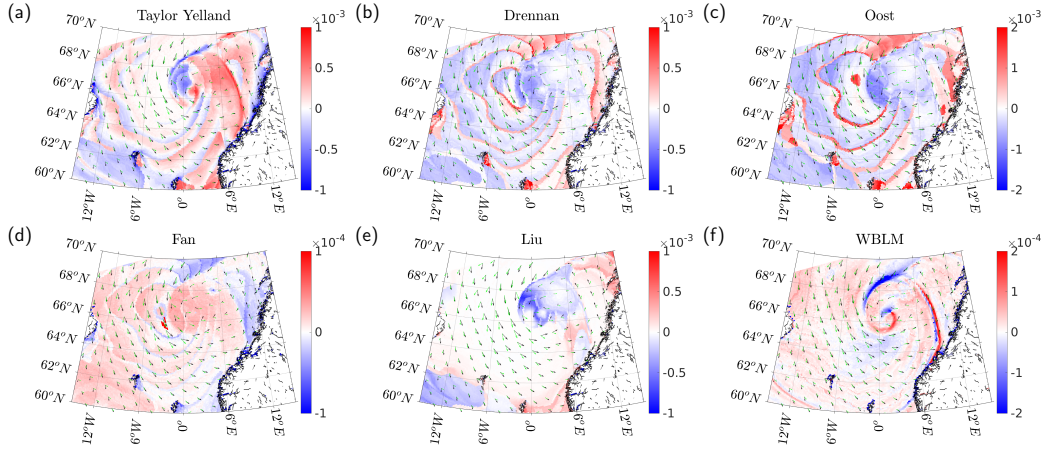


Figure 14: The difference between C_D and $C_{D,a}$ at 20:40 on the 23rd (same time as the cloud picture), around the storm center.

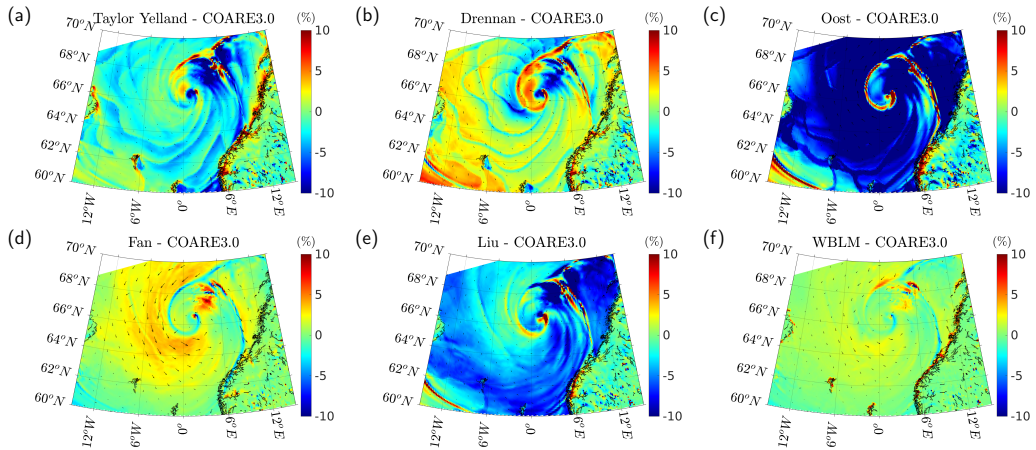


Figure 15: Percentage of deviation in U_{10} between the coupled and non-coupled modeling at the same time as Fig. 14.)

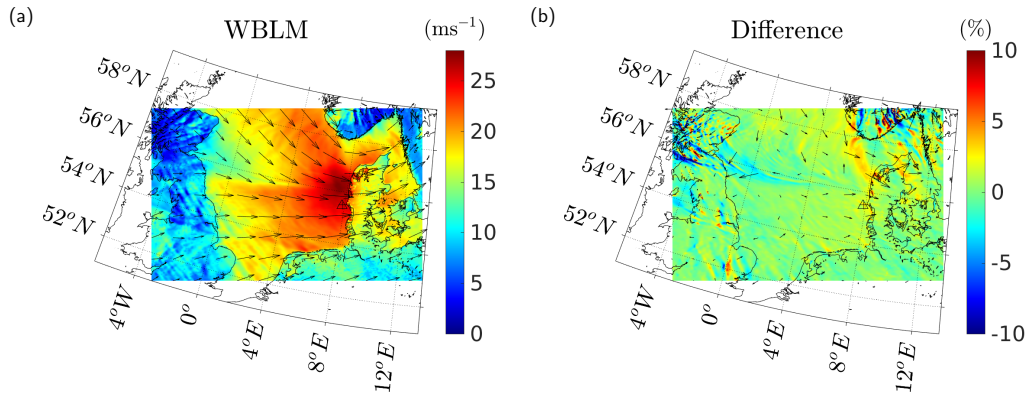


Figure 16: (a) Spatial distribution of wind speed U_{10} over domain II at 21:00, on 2002-01-28. From WBLM (b) Difference of U_{10} in percentage between using WBLM and COARE 3.0.

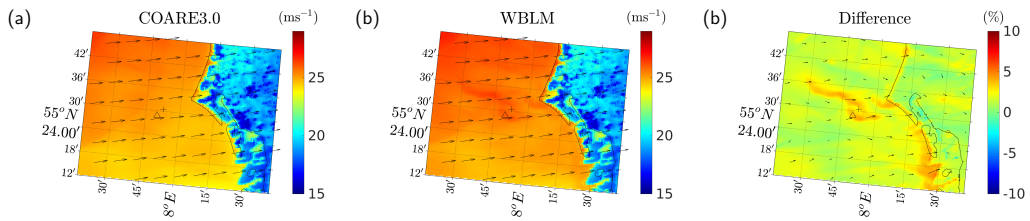


Figure 17: (a) Spatial distribution of wind speed U_{10} over domain III at 21:00, on 2002-01-28, using COARE 3.0. (b) Same as (a), but using WBLM. (c) Difference of U_{10} in percentage between using WBLM and COARE 3.0.

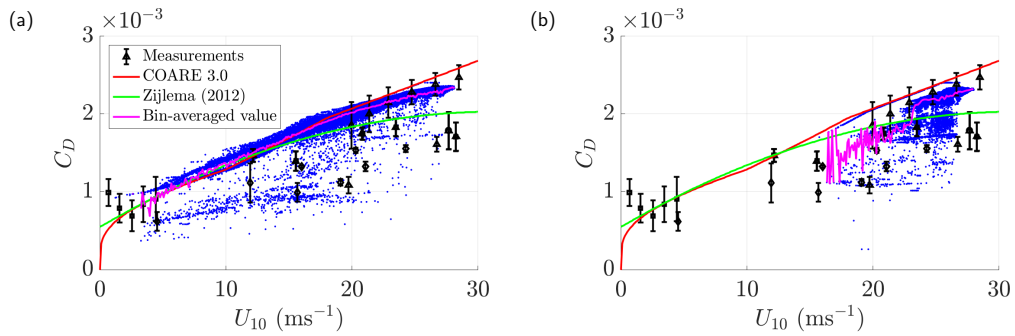


Figure 18: The distribution of C_D with U_{10} over all grid points for domain II (a) and III (b), respectively, for the data corresponding to Fig. 16.

called here the Taylor-Yelland, Drennan, Oost, Fan and Liu schemes. It is done in the COAWST system using the WRF and SWAN models. It is also the first time, the wave boundary layer model (WBLM) as implemented in SWAN in [11] is used in COAWST for real case studies.

The current study searches for an answer to the question whether the wind field is affected by waves. The answer is yes. This effect should though be classified into two types: physical and numerical.

For the physical effect, first of all, it is captured in the SAR wind field around Horns Rev 1. The SAR winds were retrieved from the surface wind wave properties, which were transferred to the wind field featuring the bathymetry. Secondly, measurements from Horns Rev 1 mast and buoy show different wave characteristics for onshore and offshore flow.

Numerically, all the five parameterization schemes and WBLM have introduced noticeable wave impact to the wind field. This is examined through a case study from 2002-02-22 and 2002-02-23 where the SAR image suggests the presence of the wave impact on the wind field. A series of atmospheric and wave parameters are examined from the coupled modelings, including u_* , z_0 , C_D , U_{10} , c_p , H_s and L_p , over the area around Horns Rev 1 (moderate winds) as well as around the storm center (strong winds). The diversity of the parameterization schemes is clearly shown when z_0 is calculated with measurements from Horns Rev 1, with the largest difference at strong winds. All schemes represent only the open sea condition at Horns Rev 1. This diversity is again shown in the COAWST modeling for case 1, leading to a difference of about 25% in U_{15} between the schemes at Horns Rev 1 M2. In general, for moderate to strong winds, the Oost scheme has largest z_0 , giving lowest wind speed; the Fan and Taylor-Yelland schemes has low z_0 , giving highest winds; the Fan scheme is closet to the uncoupled COARE 3.0 algorithm, showing mildest wave impact in the wind output. The wave impact is demonstrated, first of all, in the spatial distribution of several variables in the atmosphere model including u_* , z_0 , U_{10} and TKE , which bear the pattern of bathymetry around Horns Rev 1 as a result of bathymetry modified wave field. Secondly, the wave impact is also shown through the deviation of the individual C_D from a simple $C_D - U_{10}$ relation in the model outputs.

The wave impact is present numerically and it certainly affects the atmospheric modeling. The effect is more obvious when the wind is strong. It has been observed a difference up to XX% for U_{10} from Oost scheme (Fig. 15c). However, given the diversity of these schemes, it is needed to find out which ones are more reliable.

We examine the reliability of the many schemes from the following three aspects. Firstly, at 9:50 am 2004-02-23, over domain III the winds are light to moderate, as shown in the SAR image in Fig. 1. The effect of waves is

obvious in the wind field modeled from Taylor-Yelland, Drennan, Oost and Liu, but not visible from Fan and WBLM, see Fig. 12. Even though, Fan and WBLM, and COARE 3.0 provide winds of comparable magnitude to that of SAR data, while on average, Oost and Liu significantly underestimate the wind speed, and Taylor-Yelland and Drennan considerably overestimate it. This is consistent with the comparison made at Horns Rev 1 site. So far, the group COARE 3.0, Fan and WBLM outperform Taylor-Yelland, Oost, Drennan and Liu. Secondly, looking at Fig. 1b and Fig. 2 one can see that there is a channel with deeper water north of M2, and at M2, the winds are stronger than those in the channel. This trend is consistently present in Fan and WBLM (Fig. 10 and 17), but the oppositely in Taylor-Yelland, Drennan and Oost. Seemingly, the shallower water at M2 corresponds to smaller z_0 in Fan and WBLM but larger z_0 in Taylor-Yelland, Drennan and Oost. Of course, there is no such wave impact in using COARE 3.0. This suggests that both Fan and WBLM outperform the rest. Thirdly, the distribution of C_D with U_{10} , see Fig. 13 and 18, while Fan provides such a distribution very close to COARE 3.0, with very little spread of C_D at a certain U_{10} , it misses the range of variation of C_D collected over several water bodies. At the same time, WBLM provides such a distribution satisfactory in comparison with those measurements. WBLM outperforms the rest.

It needs to be pointed out that in the current codes of COAWST, the wave spectrum is described in discrete form with the spectral energy as a function of frequency. The energy level at the peak frequency could be comparable to that at a neighbouring frequency, thus affecting the identification of the peak frequency. This happened unfortunately in connection with the use of Taylor-Yelland, Drennan and Oost, causing artificial discontinuity of c_p at the sharp gradient of L_p , and further affecting the calculation of other parameters related, such as C_D , u_* and U_{10} see the rings of enhanced C_D and reduced U_{10} in the corresponding subplots of Fig. 14 and 15. However, this effect is organized and it did not interfere with our analysis above regarding the wave impact. The current study recommends the use of WBLM, which is free of this problem.

5 Conclusions

In the COAWST modeling system, we examined the use of different interfaces for coupling the atmospheric and wave model components and their effect on the wind field. The interfaces include two types, one is through the roughness length z_0 parameterized through wave parameters and one is through direct calculation from the wave input functions. The simulation has also been run

using WRF without coupling to the wave model. The main findings are:

- The wind fields are affected by the waves, supported by SAR data and measurements from Horns Rev 1.
- The atmospheric modeling can be significantly affected by the coupling to the wave model, in comparison with uncoupled modeling, depending on the schemes.
- It is necessary to use wind and wave coupled modeling, especially for coastal zones and for storms.
- Our method of using COAWST with WBLM in SWAN is a robust approach and it outperforms the rest approaches.
- At weak to moderate winds, the wave impact is still present as shown in the SAR data, although the modeling with WBLM may be limited in capturing this effect.

Acknowledgements This project is supported by the Danish ForskEL project XWiWa (PSO-12020). The SAR data is provided by the European Space Agency. We thank our colleagues Patrick Volker and Andrea Hahmann for their comments and suggestions.

References

- [1] S. S. Chen, W. Zhao, M.A. Donelan, and H. L. Tolman. Directional wind-wave coupling in fully coupled atmosphere-wave-ocean models: results from CBLAST-Hurricane. *J. Atmos. Sci.*, 70:3198–3215, 2013.
- [2] H. Charnock. Wind stress on a water surface. *Q. J. R. Meteorol. Soc.*, 81:639–640, 1955.
- [3] W. Drennan, J. A. Zhang, J. F. French, C. McCormick, and P. G. Black. Turbulent fluxes in the hurricane boundary layer. Part II: latent heat flux. *Journal of Atmospheric Sciences*, 64:1103–1115, 2007.
- [4] Y. Fan, S. Lin, I. M. Held, Z. Yu, and H. L. Tolman. Global ocean surface wave simulation using a coupled atmosphere-wave model. *Journal of Climate*, 25:6233–6252, 2012.
- [5] B. Liu, H. Liu, L. Xie, C. Guan, and D. Zhao. A coupled atmosphere-wave-ocean modeling system: simulation of the intensity of an idealized tropical cyclone. *Monthly Weather Review*, 139:132–152, 2011.

- [6] W.A. Oost, G. J. Komen, C. Jacobs, and C. Van Oort. New evidence for a relation between wind stress and wave age from measurements during ASGAMAGE. *Boundary-layer Meteorol.*, 102:409–438, 2002.
- [7] P. Taylor and M. J. Yelland. The dependence of sea surface roughness on the height and steepness of the waves. *Journal of Physical Oceanography*, 31:572–590, 2001.
- [8] Andreas E.L., Mahrt L., and Vickers D. An improved bulk air-sea surface flux algorithm, including spray-mediated transfer. *Q.J.R. Meteorol. Soc.*, 141:642–654, 2015.
- [9] L. Mahrt, E.L. Andreas, J. B. Edson, D. Vickers, J. Sun, and E. G. Patton. Coastal zone surface stress with stable stratification. *Journal of Physical Oceanography*, 46:95 – 105, 2016.
- [10] P.A.E.M. Janssen. Quasi-linear theory of wind generation applied to wave forecasting. *Journal of Physical Oceanography*, 21:1631–1642, 1991.
- [11] J. Du, R. Bolaños, and X. G. Larsén. The use of a wave boundary layer model in SWAN. *Journal of Geophysical Research - Ocean*, *in press*, 2016.
- [12] X. G. Larsén, C. Kalogeri, G. Galanis, and G. Kallos. A statistical methodology for the estimation of extreme wave conditions for offshore renewable applications. *Renewable Energy*, 80:205–218, 2015.
- [13] Y. Saint-Drenan. Comparison of different Charnock models for the determination of the vertical wind profile. Technical report, Fraunhofer Institut für Windenergie und Energiesystemtechnik IWES, RD Division Energy Economy and Grid Operation, Königstor 59, 34119 Kassel, Germany, http://www.hrensemble.net/public/pdf/HRensembleHR_20091221_IWES.pdf, 2009.
- [14] A. Sommer. Wind resources at horns rev. Technical report, Tech-wise A/S, 2002. Report D-160949, available online at <http://130.226.56.153/rispubl/NEI/nei-dk-4851.pdf>.
- [15] A.A.M.Holtslag and H.A.R. De Bruin. Applied modeling of the nighttime surface energy balance over land. *Journal of Applied Meteorology*, 27:689–704, 1988.

- [16] J. C. Warner, B. Armstrong, R. He, and J. Zambon. Development of a coupled ocean-atmosphere-wave-sediment transport (COAWST) modeling system. *Ocean Modeling*, 35:230–244, 2010.
- [17] M. Nakanishi and H. Niino. Development of an improved turbulence closure model for the atmospheric boundary layer. *J. Meteorol. Soc. Jpn*, 87:895–912, 2009.
- [18] G. Thompson, R. M. Rasmussen, and K. Manning. Explicit forecasts of winter precipitation using an improved bulk microphysics scheme. Part-I: Description and sensitivity analysis. *Mon. Weather Rev.*, 132:519–542, 2004.
- [19] M. J. Iacono, J. S. Delamere, E. J. Mlawer, M. W. Shephard, S. A. Clough, and W. D. Collins. Radiative forcing by long-lived greenhouse gases: Calculations with the AER radiative transfer models. *Journal of Geophysical Research*, 113:13013, 2008.
- [20] J. S. Kain and J. M. Fritsch. Convective parameterization for mesoscale models: The Kain-Fritsch scheme. The representation of cumulus convection in numerical models, Meteor. Monogr. *Ameri. Meteor. Soc.*, 24:165–170, 1993.
- [21] L. Mahrt, D. Vickers, J. Howell, J. Højstrup, J. Wilczak, J. Edson, and J. Hare. Sea surface drag coefficients in the Risø air sea experiment. *Journal of Geophysical Research*, 101:14327 – 14335, 1996.
- [22] J. Sun, D. Vandemark, L. Mahrt, D. Vickers, T. Crawford, and C. Vogel. Momentum transfer over the coastal zone. *Journal of Geophysical Research*, 106:12473 – 12448, 2001.